UNIVERSITÀ DEGLI STUDI DI PADOVA

Dipartimento di Fisica e Astronomia "Galileo Galilei"

Corso di Laurea in Fisica

Tesi di Laurea

Characterization with cosmic muons of plastic scintillators for the iMPACT project calorimeter

Relatore:

Prof. Piero Giubilato

Laureanda:

Sofia Sartore

Anno Accademico 2018/2019

Contents

1 Introduction

iMPACT, *innovative Medical Proton Achromatic Calorimeter and Tracker*, is an ERC funded project hosted by University of Padova and INFN Padova that aims to design, develop and prototype a fast scanner for proton Computed Tomography, a crucial step to improve tumors treatment effectiveness in hadron therapy. Hadron therapy is a technique where heavy ions or protons are used to target and destroy tumors, thanks to their peculiar shape in energy loss (*Bragg Peak*) that make them more precise than X-rays. Computed Tomography represents the first step of the treatment plan, where the 3D Stopping Power map of the patient body is reconstructed and used to calibrate the optimal energy and direction of the beam. Nowadays Computed Tomography is almost exclusively completed using X-rays beams, even for treatments using protons or ions; in this perspective, using the same particles with the same energy loss features both for the imaging and the treatment leads to a better aiming precision, as the physical interactions are the same. Moreover, in 2004 a study [1] proved that, in order to obtain comparable density resolutions, with pCT the deposited dose is at least 50 times lower than with X-rays CT, which is a further advantage for the patients. The main reason why proton Computed Tomography is not yet an applicable technique is the low acquisition rate of the current prototypes, that leads to scanning times of the order of tens of minutes. The goal of the iMPACT project is to assemble an extremely fast scanning system, in order to overcome the acquisition time limitation. The scanner designed for this purpose, consisting of a silicon pixels tracker and a highly segmented scintillator calorimeter, exploits leading edge technologies currently used in particle physics. During the development and prototyping phase two relevant issues, that are the focus of this thesis work, have been investigated and assessed. The first issue is to find the best wrapping method for the scintillators, in order to maximise the light collection and minimise the cross-talk between adjacent scintillators, while meeting a low material budget constrain. The second goal is to parametrise the dependence of a single detector's response with respect to the position of the incident particles, in order to verify the response uniformity inside the whole volume of the calorimeter. These studies were conducted with the iLDA (*iMPACT Labview Data Acquisition*) setup: a ready-to-use desktop system, developed within the iMPACT framework, which exploits cosmic muons as a reliable, easily accessible, repeatable and well-known signal source to generate reference datasets. This setup allows to easily carry out tests and characterizations on different candidate detector components for the realization of the iMPACT scanner. This thesis work begins discussing the limitations and advantages of hadron therapy with respect to X-rays therapy, focusing of the interactions of protons with matter. The current state of the art of proton Computed Tomography scanners and different concepts of calorimeters are presented, followed by the description of iMPACT project's scanner. The functioning principle of the SiPM technology used in the project is introduced, as well as the Geant*4*-based simulation tool specifically developed to study and predict the calorimeter behaviour. The iLDA data acquisition system is then described, followed by a quick overview on cosmic rays and in particular on cosmic muons used for the purpose of this thesis work. The last section of the thesis focuses on the experimental procedure and the obtained results are presented.

2 Proton tomography

Nowadays tumors are one of the main causes of death in economically developed countries [2]; until recent days the ways of treating them mainly rely on surgery, chemotherapy and X-rays therapy [3]. In the latter procedure, a beam of X-rays is delivered to the affected area in the patient's body; X-rays are generally produced by accelerating a stream of electrons and colliding them with a metal target. High-energy photons produce secondary electrons in human tissue, causing DNA damage which, if not repaired, is fatal at cell reproduction. The *dose* of radiation is defined as the energy absorbed per unit mass by tissues, usually expressed as grays, Gy (1 Gy = 1 J/kg). The dose is usually delivered in a number of daily fractions, with the total dose determined by tumour sensitivity and normal tissue tolerance. The problems with using X-rays radiation are mostly related to the fact that once it penetrates the matter, the radiation releases its maximum energy within few centimeters under the surface, as shown in Fig. 1, and therefore it is difficult to irradiate the actual target volume without damaging the healthy tissues nearby. This issue becomes particularly relevant when the tumor is deeply located inside the body, which is the case for many tumors, and the volume that needs to be irradiated is close to vital organs. It is therefore very beneficial to find alternative, less damaging solutions; these are offered by therapy with hadrons, such as protons and heavier ions, that are characterized by a shape in energy loss much more convenient for cancer treatment than X-rays.

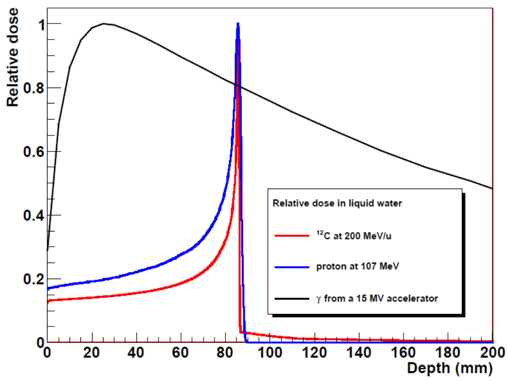

Figure 1: Comparison of the dose depth profile in water for carbon ions, protons and X-rays [4].

The energy loss profile (*Bragg curve*) of hadrons of given energy features a progressive increase followed by a maximum as they come close to rest, called *Bragg peak*, and goes to zero within few centimetres, as shown in Fig. 1. The first part of the energy loss profile, called *protonic buildup*, features an average dE/dx which is 20% to 30% of the Bragg peak. This peculiarity can then be exploited in medical applications such as cancer treatment: thanks to the Bragg peak, with *hadron-therapy* the majority of the released energy can be confined to the cancer volume, minimizing collateral effects to healthy tissues [3]. Moreover, it is possible to control the depth the beam reaches by adjusting its energy, making it possible to realise a precise 3D coverage of the tumor volume (*beam painting* technique [4]).

2.1 Interaction of protons with matter

Protons in the energy range suitable for hadron-therapy, 150 to 250 MeV, interact with matter mostly through Coulomb inelastic scattering with outer shell electrons of the target atoms and Coulomb elastic scattering with nuclei; nuclear scattering is also possible although it accounts for only 10% of the total energy loss [5] Protons travel through matter in approximately straight lines, they continuously slow down and deflection angles due to Coulomb scattering are small as protons are much more massive than electrons. The *mean energy loss per unit length* due to Coulomb interactions with electrons of the target is called *Stopping Power* (S_p) and it is described by the Bethe Bloch formula [6] :

$$S_p = -\left\langle \frac{dE}{dx} \right\rangle = \frac{4\pi}{m_e c^2} \cdot \frac{nz^2}{\beta^2} \cdot \left(\frac{e^2}{4\pi\varepsilon_0}\right)^2 \cdot \left[\ln\left(\frac{2m_e c^2\beta^2}{I\cdot(1-\beta^2)}\right) - \beta^2 - \frac{\delta}{2} - \frac{C}{Z}\right] \tag{1}$$

where m_e is the electron mass, z is the the particle electric charge, β is the particle speed in units of c, I is the mean excitation potential of the material, δ is the outer electrons shielding correction, C is a shell-correction parameter and n the electron density. It is usual to scale the stopping power with respect to water in radiobiological contexts, defining the *Relative Stopping Power* (RSP) as:

$$\mathrm{RSP} = \frac{{S_p}^{\mathrm{material}}}{{S_p}^{\mathrm{water}}} \tag{2}$$

where ${S_p}^{\mathrm{water}}$ is the stopping power in water [7]. The average depth in a material at which the particles stop is called *range*. Because of the continuous slowing down, ions have a much more defined range than other types of radiation, such as electrons. The range R of a beam with starting energy E, whose path is ideally strictly linear, can be calculated as

$$R(E) = \int_0^E \left\langle \frac{dE'}{dx} \right\rangle^{-1} dE' \approx \alpha E^p \tag{3}$$

where the latter equivalence is an empiric parameterisation (*Bragg-Kleeman rule*) with α and p parameters that depend on absorber and particle and must be inferred experimentally [8]. Range describes an average behaviour, since the single inelastic Coulomb scattering of the incident particle with electrons has a stochastic nature. Summing over a wide number of collisions with electrons leads to statistical fluctuations of the energy loss rate, causing a spread of the particles stopping position around the mean range. This spread is called *range straggling* and it can be seen as a broadening of the Bragg peak in the energy loss profile. The precision of predictions and measurements of particle ranges is limited by the range straggling; the tabulated values of range and range straggling for particles at different energies show that for protons around 200 MeV the relative range straggling stands between 0.9 and 1.2% [9].
The Coulomb interactions of protons with the nuclei of the target material are not responsible for a significant energy loss; instead, they cause the deviation of the particles from their linear path, as formulated in the Rutherford single scattering theory; however in the typical clinical case, a Multiple Coulomb Scattering (MCS) theory is necessary, due to the thickness of the tissues; such a theory was proposed by Molière [10]. For instance, a 230 MeV proton passing through 20 cm of water is deviated with an average angle of about 1.9°.

2.2 Proton tomography

In order to evaluate the depth of the Bragg peak needed for the treatment, it is necessary to know the Stopping Power of all the tissues along the beam path. Having a precise body Stopping Power map is therefore fundamental, as it determines the accuracy of the treatment. Nowadays, for all kinds of radiation therapy, this 3D map is realized with *X-rays Computed Tomography* (X-rays CT): a rotating photon beam invests the scanned object, while a detector positioned on the opposite side measures the intensity of the beam, producing a 2D photon absorption map for each imaging slice. The data are then analyzed with a reconstruction software, which eventually provides a photon absorption 3D map expressed in *Hounsfield Units* (HU), which are defined as:

$$\mathrm{HU} = 1000 \cdot \left(\frac{\mu - \mu_{\mathrm{water}}}{\mu_{\mathrm{water}} - \mu_{\mathrm{air}}}\right) \tag{4}$$

where μ is the linear attenuation coefficient in a given position inside the object, μ_{water} and μ_{air} are the water and air attenuation coefficients. For proton-therapy, an equivalent Stopping Power map must be

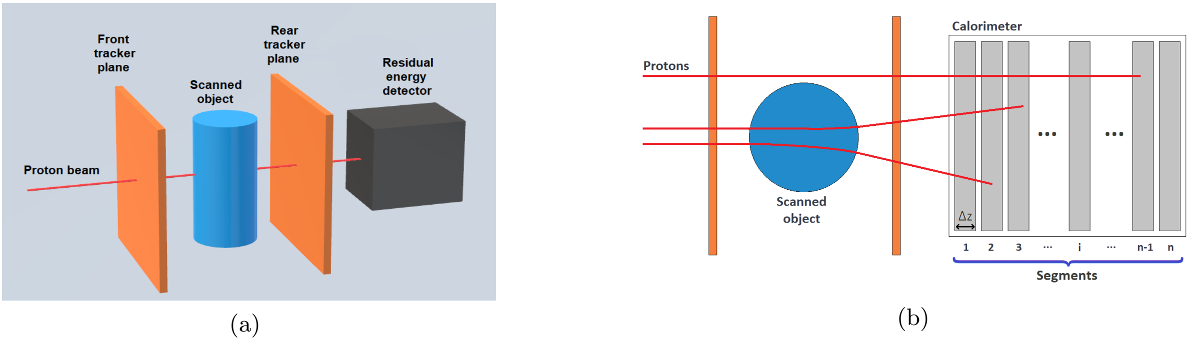

Figure 2: (a) Schematic representation of typical pCT scanner layout. (b) Schematic view of a pCT scanner with segmented calorimeter [14].

extrapolated [11]. However, the uncertainties on the proton range obtained with this procedure span between 5% and 2%, which are at best twice the intrinsic theoretical limit of 1%, given by the range straggling [12]. This is mainly due to the different behaviour of photons and hadrons inside matter, leading to a non univocal correlation between the HU and the RSP. Therefore, it would be more convenient to get the RSP directly from the protons energy loss information, without having to use the conversion from HU. This would in fact provide a more accurate proton range prevision and eventually a more effective treatment plan, since the same particle is used for both imaging and treatment. The procedure consisting in using protons for imaging purposes is known as *proton Computed Tomography*, or pCT. A further advantage in using this procedure is that it is possible to use the same facility both for the imaging and the treatment: this, besides resulting in a significant cut in costs, also contributes to the effectiveness and comfort of the treatment by administering both services in the same session. Moreover, pCT is convenient also in dose deposition terms, as the deposited dose is considerably lower than the deposited dose using X-rays CT. Different prototypes are currently under study and realised around the world [7]. The present prototypes consist usually of a tracking system, made of either position sensitive $\hat{x}-\hat{y}$ Silicon Strip Detectors planes or $\hat{x}-\hat{y}$ Scintillating Fiber planes, to measure the position and direction of entering and exiting protons, and a dedicated detector for the measurement of their residual energy. Scintillator-made *calorimeters* are almost exclusively used for this purpose, for their fast response and possibility to cover large volumes. The RSP map is eventually computed combining the measurements of energy and tracking of every single proton [13]. As this thesis work concerns the characterisation of components of the calorimeter, a detailed description of the tracker is omitted in this place in favor of a focus on the former. The quantity that one aims to retrieve from the calorimeter is the proton path length inside the scanned object. The *Water Equivalent Path Length* (WEPL) is a standard parameter that can be expressed as the integral of the relative stopping power RSP along the proton path L inside the adsorber material:

$$\text{WEPL} = \int_L \text{RSP}(\ell)d\ell \tag{5}$$

where RSP(ℓ) is the relative stopping power at ℓ distance along the path. The WEPL is preferred over an energy loss measurement because it is more explicitly related to the RSP [15].
Usually, a pCT energy detector calorimeter can be generalized as $n \geq 1$ consecutive scintillator layers aligned in the direction of the beam $\hat{z}$; each scintillator layer has a water equivalent thickness Δz, as shown in Fig. 3 (b), the total calorimeter thickness $n\Delta z$ being enough to stop all the protons. The WEPL inside the scanned object of a monoenergetic proton beam with a total range in water R_{tot}, as defined in Eq. (3), can be estimated by:

$$\text{WEPL} = R_{\text{tot}} - R \tag{6}$$

where R is the water equivalent distance travelled by protons within the calorimeter volume. The uncertainty sources affecting this estimate of WEPL are the intrinsic range straggling (σ_R^{stragg}) and

the experimental uncertainty (σ_R^{exp}), the total uncertainty on a measure of WEPL (σ_{WEPL}) being the square root of the quadratic sum of the two terms. In order to reach the theoretical limit of $\sigma_{\text{WEPL}} \sim \sigma_R^{\text{stragg}}$, the experimental term has to be small with respect to the straggling term, for a wide range of WEPL values. There are different calorimeter configurations that can be used to obtain a WEPL measurement. In case of a single-volume calorimeter, i.e. $n = 1$, the protons residual energy is measured, and its range has to be inferred with the Bragg-Kleeman rule (3). The experimental uncertainty in this case can be derived from the Bragg-Kleeman rule: $\sigma_R^{\text{exp}} = p(R_{\text{tot}} - \text{WEPL})\delta E$. The energy resolution δE of the calorimeter must be better than 1% for a large range of energies in order to meet the needed precision on range. This is a challenging requirement for the construction of a calorimeter which needs to be fast as well.
Alternatively, a *range counter* can be used to estimate WEPL: in this case, the calorimeter is composed by a large number of layers ($n \gg 10$) and a binary 'hit or miss' output is used to determine whether a layer was crossed or not, with response based on the excess of the signal over a chosen threshold. The range R of a proton is deduced by the number of calorimeter layers $\bar{i}$ that recorded a signal over threshold. The WEPL estimation from Eq. (6) becomes:

$$\text{WEPL} \approx R_{\text{tot}} - (\bar{i} - 1)\Delta z - \frac{\Delta z}{2} \tag{7}$$

assigning the center of the last layer hit as a reasonable guess of the proton stopping position. In this case the experimental uncertainty is simply the thickness of the layer divided by $\sqrt{12}$. The requirement of the experimental contribution to σ_{WEPL} being negligible is then substantially met if $\Delta z < 0.015 \times R_{\text{tot}}$, which is approximately 4 mm for 200 MeV protons, with no particular requirements on the energy resolution. Moreover, a range counter represents a much simpler solution, in terms of operations, with respect to an energy calorimeter. The need of a single energy threshold on each channel, in fact, removes the necessity of a precise and repeated calibration and simplifies the readout process.

2.3 Current limitations

Unlike X-rays CT, proton tomography is not yet an easily practicable technique, as there are physical, technological and accessibility limitations: first of all, the multiple coulomb scattering is responsible for a spatial resolution that is worse than that of the X-rays CT [16]. Moreover, at this stage the experimental acquisition rate of the pCT prototypes is quite slow (a complete record of the necessary information would take about 10 minutes to be completed), but having a better quality of the images requires the patients to be completely still and hold their breath to avoid motions of internal organs and for this purpose the ideal maximum acquisition time for the scanning is around 10 s. Lastly, the high cost of construction, operation and maintenance of the facilities for hadron-therapy, with which the pCT procedure would be applied, limits their diffusion: despite the fast growth of the number of these centers, the fact that the cost for a proton treatment would be approximately twice the cost of a photon treatment makes the latter be the most common procedure nowadays [17]. The instrumentation needed for pCT has high costs as well, mainly as it has not yet proceeded from the prototyping phase to the engineering one.

3 iMPACT project

iMPACT is a European ERC funded project (Consolidator Grant 649031) that aims to build a *proton Computer Tomography scanner* which overcomes some of the technological limitations mentioned above [18]. The goal of the project is to offer a competitive solution in terms of material, instrumentation and running costs while at the same time obtaining a high resolution and short acquisition time, in order to meet the clinical viable acquisition rate limit of recording 10^9 proton events in about 10 s. To do this, the project exploits technologies currently in use for particle physics detectors, such as the *Monolithic Active Pixel Sensors* ALPIDE the ALICE collaboration developed for the upgrade of its

Inner Tracking System; this design was preferred over other solutions mainly for its higher acquisition rate capability and lower material budget [19]. The current design of the scanner employs a tracker and a calorimeter: the tracker is made of 4 ALPIDE sensors tracking planes, two upstream and two downstream the scanned object; the calorimeter is finely segmented in the $\hat{z}$ direction into 5 mm layers of plastic scintillator elements, called fingers. Such fingers are alternately oriented along the $\hat{x}$ and $\hat{y}$ axis, allowing to track multiple protons simultaneously and therefore improving the maximum allowed particle rate (see Fig. 3).

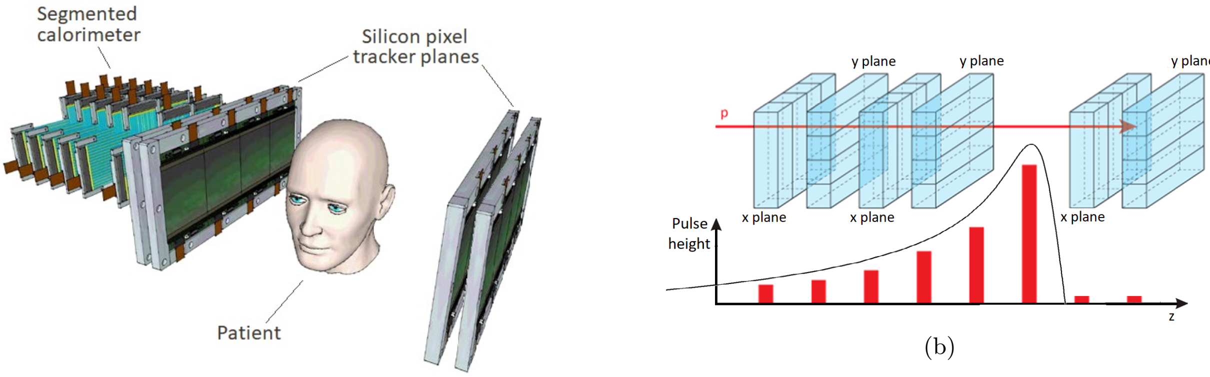

(a) (b)

Figure 3: (a) Rendering of the iMPACT project scanner layout [14]. (b) iMPACT calorimeter layout, segmented in alternate $\hat{x}$ and $\hat{y}$ layers. Red bars represent the expected signal amplitudes along the layers [18].

The iMPACT calorimeter is proposed to be an improved version of a range counter: in fact the primary measured quantity is the path length of each particle inside the detector, however the deposited energy signals will be used to improve the range estimate. In fact, while on one hand the stopping position can be roughly estimated simply observing the depth of the last layer that recorded a signal, on the other the output signal amplitudes along the planes can be used to reconstruct the shape of the proton Bragg curve, which can then be fitted in order to improve the proton stopping position estimation, achieving a resolution better than the one given by the layer thickness.
The iMPACT hybrid energy-range calorimeter foresees $n \approx 60$ layers, with thickness $\Delta z = 5$ mm. The knowledge of the $\bar{i}-$th layer where the proton comes at rest limits the position in the interval $[(\bar{i}-1)\Delta z\ ;\ \bar{i}\Delta z]$, while the energy deposited in the layers can be used for an improved estimate of the proton stopping position inside the $\bar{i}$-th layer, as can be seen in Fig. 4. The *probability density function* (*pdf*) of a variable with known lower and upper limit, $z_{\min}$ and $z_{\max}$ respectively, and an educated guess on the most likely value $\hat{R}$ (mode) is the triangular distribution, also known as the *lack of knowledge* distribution. The variance of a triangular distribution is given by:

$$\left(\sigma_R^{\exp}\right)^2 = \left(\sigma_R^{\text{triang}}\right)^2 = \frac{{z_{\min}}^2 + {z_{\max}}^2 + \hat{R}^2 - z_{\min}z_{\max} - z_{\max}\hat{R} - z_{\min}\hat{R}}{18}. \tag{8}$$

Fig. 4 shows the different contributions to σ_{WEPL} predicted for the iMPACT calorimeter. The experimental uncertainty σ_R^{triang} (red line) oscillates between 1 and 1.5 mm, almost 1/3 of the intrinsic straggling term $\sigma_R^{\text{stragg}} = 0.011 \times (R_{\text{tot}} - \hat{R})$ which is about 2.8 mm (blue line), so the total WEPL uncertainty σ_{WEPL} (green line) is dominated by the latter. The total WEPL resolution is expected to span between 3 and 3.2 mm, close to the theoretical limit of 2.8 mm given by the intrinsic fluctuations of the physic process, so further improvements on the experimental resolution would not lead to a substantial improvement of the total WEPL resolution. It is also worth to recall that σ_R^{triang} is also smaller than the resolution of the iMPACT calorimeter when used as a simple range counter, i.e. neglecting the energy information, in which case $\sigma_R^{\text{counter}} = 5\text{ mm}/\sqrt{12} \approx 1.4$ mm. More details on the expected resolution of the iMPACT calorimeter can be found in [14]. An early prototype of the calorimeter has been tested with proton beams from 3.5 MeV to 228 MeV, results can be found in [14],[20],[21].

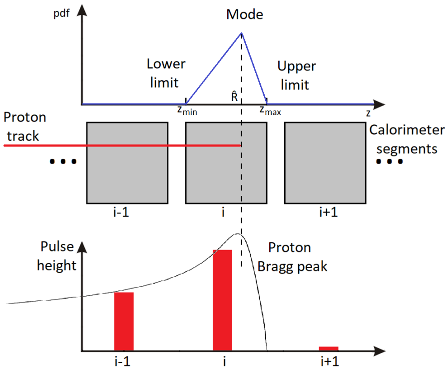

(a)

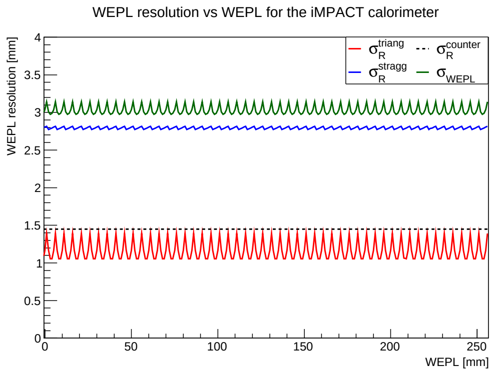

(b)

Figure 4: (a) Concept of a hybrid calorimeter, exploiting both range and energy information. The *probability density function* describing the knowledge of the proton stopping position, based on energy deposition in the calorimeter layers, is the triangular distribution. (b) Foreseen WEPL resolution of the iMPACT calorimeter as a function of WEPL (green line) [14]. The experimental term from Eq. (8) σ_R^{triang} (red line) and the intrinsic uncertainty due to straggling (blue line) are shown as separate contributions. The expected experimental resolution when the iMPACT calorimeter is operated purely as a range calorimeter is shown as well (black dashed line).

3.1 SiPM technology

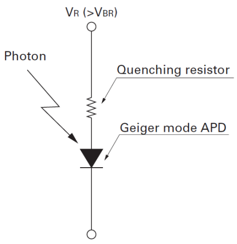

(a)

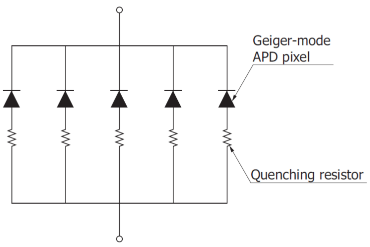

(b)

Figure 5: (a) Geiger mode APD (Avalanche PhotoDiode) and quenching resistor. V_R: Reverse voltage, V_{BR}: Breakdown voltage. (b) The configuration in parallel of multiple APD to form a SiPM [22].

Each scintillator composing the iMPACT calorimeter is coupled to a Silicon Photo-Multiplier (SiPM), which converts the optical scintillation photons into an analog voltage signal. A SiPM is a solid state photon-counting device, developed for low light level detection, and intended to be an alternative to Photo-Multiplier tubes (PMT). These devices provide high photon detection efficiency, up to 40%, active area smaller than cm^2, low operating voltage (around 60 V), below-ns timing response, good time resolution, up to 250 ps, wide spectral response range [22]. A SiPM is made up of multiple independent Avalanche PhotoDiodes (APD) operating in Geiger mode: a reverse voltage, higher than the breakdown voltage, is applied to each APD, so that even the charge induced by a single photon can result in a Geiger avalanche discharge. In this condition the output current of each APD is constant and independent from the released charge. The APD is blind to photons incoming during the discharge process, so a quenching resistor is included in series with the APD in order to stop the discharge. The time that is necessary to the APD to be capable of detecting new photons after a photon hit is called quenching time t_{quench}.
A number of APD and quenching resistors are connected in parallel to form the surface of a SiPM, as in Fig. 5 (b), so that the resulting signal of the SiPM is the pile-up of the signal from each APD. The detection of multiple photons results in a total signal which is proportional to the number of

photodiodes hit. The relation between the signal amplitude and the number of detected photons is linear as long as the number of simultaneous photons is low enough to have a negligible probability for two or more photons to hit the same APD.
SiPM photon detection efficiency depends on different factors, such as quantum efficiency, fill factor and avalanche probability, and is generally dependent on the wavelength of the incident photon. Hamamatsu S12572-025c, with 25 µm APD pitch over a $3\times3\,\text{mm}^2$ area, have been chosen for the iMPACT calorimeter. A measured waveform produced by a SiPM of the said model is presented in Fig. 6 (a), while the photon detection efficiency as a function of wavelength is shown in Fig. 6 (b); in the same plot the light output distribution of the PVT scintillator considered (Saint-Gobain BC-408) is also presented. The photon emission spectrum is well within the area of the maximum efficiency of the SiPM.

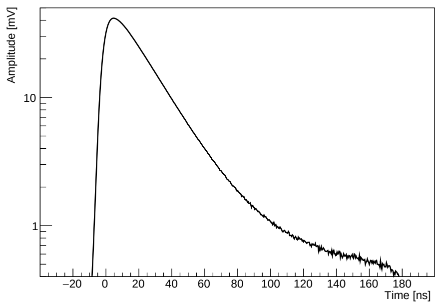

(a)

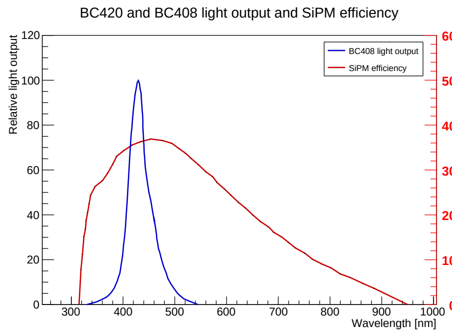

(b)

Figure 6: (a) Example of a measured signal of a HAMAMATSU S12572-025c SiPM with no front-end electronics. (b) Scintillator (BC408) light output as a function of the wavelength (primary axis) compared to SiPM detection efficiency (secondary axis). Data retrieved from Hamamatsu and Saint-Gobain data sheet [22],[23].

3.2 Simulation

To evaluate the performance of the calorimeter, a Monte Carlo simulation was developed, using the GATE application [24], based on the Geant*4* toolkit [25]. The simulation consists of a single scintillation volume with the dimensions of the scintillators used in the calorimeter. The material of the volume is defined as polyvinyl toluene; the optical characteristics of the materials and the surfaces are parameterised to simulate the optical behaviour of a scintillating detector with a highly reflective teflon wrapping. In GATE, different particle sources can be defined, to simulate either tests with protons or cosmic muons, with customizeable energy spectrum and source geometry. As a particle travels in the sensitive volume, its energy loss is simulated, according to the Geant*4* libraries, and along its path, a number of optical photons, proportional to the energy loss, is generated isotropically; the wavelength spectrum of the emitted photons is parameterized as in Fig. 6 (b). The optical photons processes, such as their propagation and absorption in the material, as well as the interaction with the surfaces, are simulated. On one of the end-faces of the scintillator a model of the SiPM is placed, featuring a detection efficiency parameterised as a function of the photon wavelength, as in Fig. 6 (b). Photons reaching the SiPM surface and selected according to the parameterised efficiency are considered as 'detected photons'. The information on the photons collected on the SiPM is then used to retrieve an equivalent of the analog voltage signal: the total SiPM signal is generated as the pile-up of a single APD cell signal for each detected photon. Details on the Monte Carlo code, the signal reconstruction and the measurement of the single APD cell signal can be found in [14].

3.3 The iLDA setup

The desktop-based and GUI-driven iLDA data acquisition setup was developed within the iMPACT project. iLDA exploits cosmic muons to characterize and calibrate a detection system based on scintillators. The setup consists of up to four scintillation detectors, each coupled to a read-out electronic channel through a SiPM; a custom Labview based software has been developed for this application; the software is used to acquire the data, by controlling, via USB, an oscilloscope (4 channels, 2.5 GS/s), providing real-time acquisition diagnostics, and store each waveform in a text file, allowing to perform offline analysis. Moreover, different trigger logics can be implemented through the software, combining the available trigger channels, and the system is designed to independently run the long-duration acquisition, necessary to acquire an adequate number of events. To detect cosmic rays but minimize the noise from external light, the setup was optically insulated by means of a box and a thick, dark cloth. In the frame of this work, iLDA was used to study different configurations of the scintillators wrapping and to characterize the output signal dependence on the particle hit position on the scintillator, which is essential to map the response uniformity of the complete calorimeter volume.

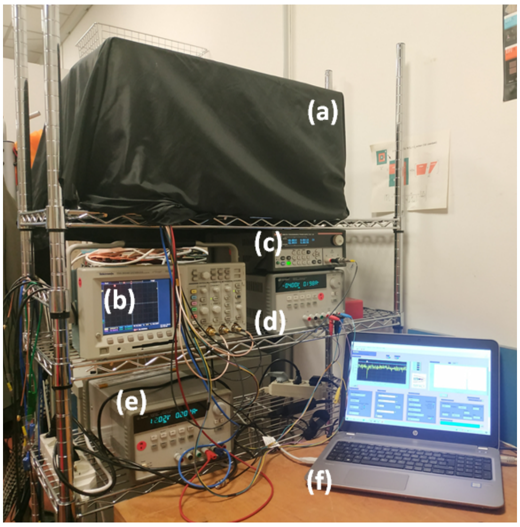

Figure 7: Photo of the entire iLDA apparatus: (a) dark box in which the scintillators are placed; (b) Tektronix TDS3034B Oscilloscope (4 channels, 300 MHz, 300 MHz, 2.5 GS/s); (c) Keithley 2200-72-1 Programmable Power Supply for SiPM bias; (d) Keysight E3631A for read out electronics power supply; (e) Agilent E3631A Power Supply for PMT bias; (f) Computer with LabView software.

3.4 Cosmic rays

We address as Cosmic Rays all kinds of radiation from extraterrestrial sources. They were discovered in the first decades of 20^{th} century and owe their name to Millikan [26]. Their energy distribution is approximated by a power law E^{-p}, with p typically between 2.7 and 3.3. In the actual energy spectrum there are three main changes of slope that are called respectively knees and ankle; the most accredited interpretation of these changes in slope is that they mark different regions, corresponding to different sources of cosmic rays (solar, galactic, extragalactic). Cosmic rays are classified as primary or secondary: primary cosmic rays are the original particles with extraterrestrial origin; most of high energy particles in primary cosmic rays are protons, roughly 10% are alpha particles and approximately 1% are heavier nuclei or neutrons. The remaining 1% of cosmic rays are electrons and neutrinos. Collisions of primary cosmic rays in the atmosphere produce cascade events, called showers, that generate secondary particles. In particular, high energy primary hadrons colliding with nuclei generate mostly pion mesons, but also neutrons, protons, antiprotons, antineutrons, heavy mesons and hyperons. Charged pions almost exclusively decay into muons $\pi^{\pm} \rightarrow \mu^{\pm} + \nu_{\mu}$ with mean lifetime τ=2.6×10^{-8}

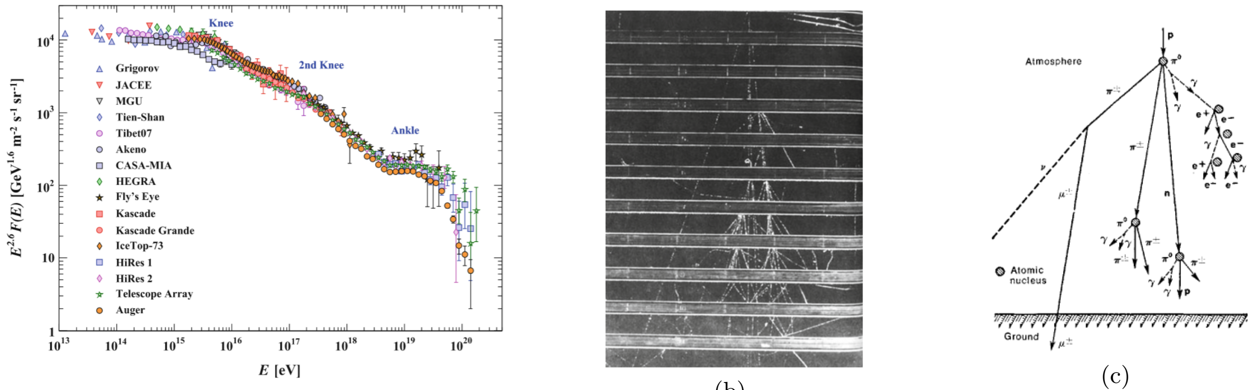

(a) (b) (c)

Figure 8: (a) Cosmic-ray spectrum coming from experimental measurements by different experiments; the spectrum has been multiplied by $E^{2.6}$ [26]; (b) Image of a hadronic shower developing through a number of brass plates 1.25 cm thick placed across a cloud chamber [27]; (c) Scheme of a cosmic ray shower: the primary particle (usually a proton) collides with a nucleus in the atmosphere. The products include neutrons, protons, neutral and charged π mesons, antiprotons, antineutrons, heavy mesons and hyperons. Neutral mesons decay into gamma rays, wich generates electromagnetic showers [28].

s, while neutral pions mostly decay into two photons $\pi^0 \rightarrow \gamma\gamma$ (τ=8.4 $\times$ 10^{-17} s) and can start electromagnetic showers. Muons can then decay into electrons, positrons and neutrinos $\mu^{\pm} \rightarrow e^{\pm} + \nu_{\mu} + \nu_e$. In particular, secondary muons have a lifetime that is long enough to reach the Earth's surface (τ=2 $\times$ 10^{-6} s). Charged particles at sea level are in fact mostly muons and some high-energy muons even penetrate for some kilometres inside the surface. Fig. 9 (a) shows the muon momentum spectrum at sea level at 0° zenith angle [29]. The mean momentum of muons at the ground is approximately 4 GeV/c. The momentum spectrum is almost flat below 1 GeV/c, steepens gradually to reflect the primary spectrum in the 10–100 GeV/c range, and steepens further at higher energies because pions with $E_{\pi} > 100$ GeV/c tend to interact in the atmosphere before decaying. Asymptotically ($P_{\mu} \gg 1$ TeV/c), the energy spectrum of atmospheric muons is one power steeper than the primary spectrum. The overall zenith angular distribution of muons at the ground is proportional to $\cos^2\theta$, as shown in Fig. 9 (b).

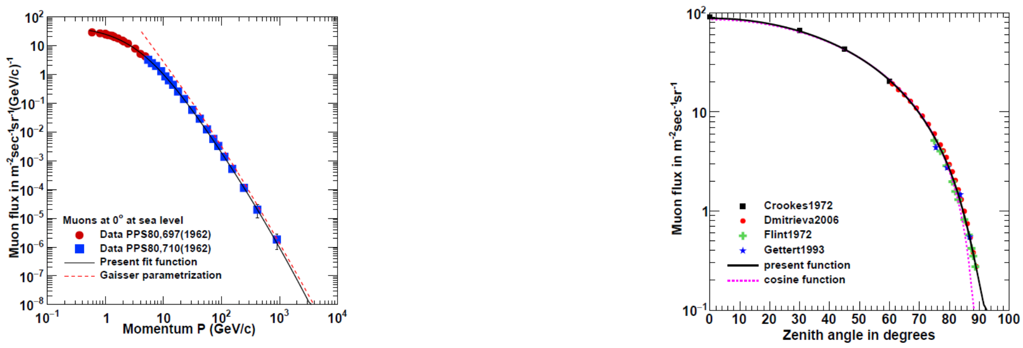

(a) (b)

Figure 9: (a) Muon momentum distribution at 0° zenith angle at sea level. (b) Muon flux as a function of zenith angle at sea level [29].

Cosmic muons, having a mean momentum around 4 GeV/c, can be identified as *minimum ionizing particles*, which means they have a mean energy loss rate close to the minimum within less than a factor of two. When fast charged particles pass through absorbers that are thin compared to their range, the distribution that describes the energy loss is asymmetric and is called *Landau distribution* [30]; in this distribution, the most probable value is smaller than the mean value, represented by the Bethe formula, because of the tail in the Landau distribution towards higher energies. For particles such as electrons and positrons, energy loss is also due to Bremsstrahlung, but for heavier particles as muons or protons, this effect is not relevant until high energies (for muons radiative effects reach 1% of the total energy loss at $E \sim 100$ GeV), that are not concern of this study (Fig. 10).

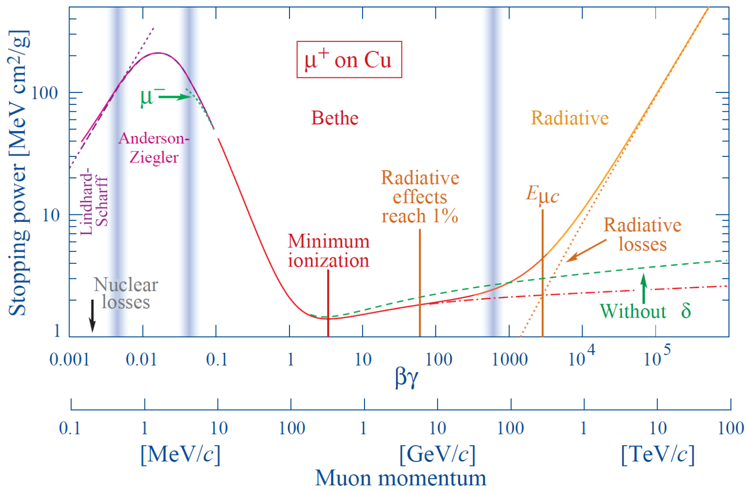

Figure 10: The stopping power ($-dE/dx$) for positive muons in copper as a function of $\beta\gamma = p/Mc$ is shown over nine orders of magnitude in momentum (corresponding to 12 orders of magnitude in kinetic energy) [31].

4 Experimental procedure

One of the goals of this thesis work was to find the wrapping configuration that minimises the cross-talk between adjacent scintillators while at the same time avoiding an excessive thickness of the wrapping itself. The other task was to investigate the uniformity of the response of a single scintillation finger, as a function of the particle incident position. The results of these measurements can be used to verify the uniformity of the response in the volume of the calorimeter and at the same time to parameterise the response to be exploited in simulations of the entire apparatus.

4.1 Cross-talk setup and analysis

One of the key elements of the calorimeter mechanical design is the external wrapping of the scintillating fingers, which should provide a good reflectivity and low optical absorption on the internal surface, to ensure the proper collection of the scintillation photons. However the wrapping in its entirety has to be opaque to optical photons, to provide optical isolation between adjacent scintillators. At the same time the wrapping layers have to be as thin as possible. This layers, in fact, act as passive material inside the calorimeter, resulting in both undetected energy loss and blind spots between the scintillators that are juxtaposed, side by side, to form a plane.

A dedicated configuration of the iLDA setup was used to study the optical cross-talk between adjacent scintillators, with four scintillator fingers arranged in two rows, each with two fingers in contact with each other, as shown in Fig. 11. The upper row consists of the two fingers identified as 1 and 3, while the lower one groups fingers 2 and 4. The setup is equipped with two readout boards, handling signals from fingers 1 and 2, and 3 and 4, respectively. The readout boards were checked for uniformity in voltage gain among different channels before starting the measurements, and the replacement of few components was required. The read out electronics was connected to the 4-channels oscilloscope. The trigger logic was set to accept events producing simultaneous signals in two scintillators vertically aligned with each other (i.e. scintillators 1 with 2 or 3 with 4), to select particles moving almost

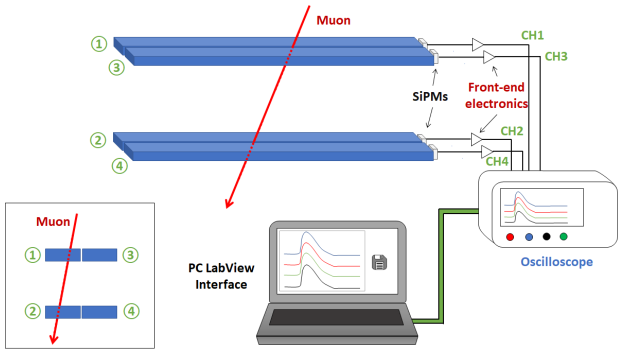

(a)

(b)

Figure 11: (a) Schematic representation of the iLDA cosmic muon setup, used in the configuration for the cross-talk studies: the scintillators are labelled from 1 to 4; in the box a horizontal view is shown; (b) a photo of the setup in the said configuration.

perfectly along the vertical direction. Different configurations were studied to determine the best wrapping for the scintillators to minimize the cross-talk effect. Two sets of data were acquired for every wrapping configuration: one with the trigger on the coincidence of channels 1 and 2 and the other with the trigger on channels 3 and 4. The decision of taking data sets with two specular trigger logics was made to minimise the effects of individual SiPM manufacturing, output or efficiency, disuniformities in finger wrapping or light output, and manual assembly of the components. The following wrapping configurations were investigated:

- configuration a (c_a) – the four scintillators were all uncovered, to study a configuration were the cross-talk is maximum;
- configuration b (c_b) – the triggered scintillators were uncovered, while the other two scintillators were wrapped in aluminum and the sides facing the SiPMs were covered with black tape in order to prevent them from detecting scintillation photons. This configuration provides a background reference, where the optical cross-talk is eliminated, and just the electronic cross-talk between two adjacent electronics channels may be visible;
- configuration c (c_c) – all four channels were randomly triggered with an external function generator, to measure the electronics noise and SiPM dark count;
- configuration d (c_d) – triggered scintillators are uncovered. The non triggered scintillators are wrapped in aluminum and their corresponding SiPM are removed, to monitor the influence of the SiPMs on the total background noise;
- configuration e (c_e) – one teflon layer separates the adjacent scintillators;
- configuration f (c_f) – two teflon layers separate the adjacent scintillators;
- configuration i (c_g) – each scintillator is wrapped in a single teflon layer and an aluminum layer separates adjacent scintillators.

The data acquired for each different configuration were analysed through a ROOT macro, used to identify the maximum voltage amplitude of each event waveform, create histograms, apply cuts to the data set and further analyse them. In Fig. 12 average waveforms for the four channels are shown, for two particular data sets. For configuration c_a (Fig. 12 (a)), with all scintillators uncovered, there is an evident peak in the average waveforms of untriggered channels (CH3 and CH4) in correspondence with the peak of the main signal average waveforms (CH1 and CH2): this is evidence of a not negligible cross-talk between adjacent scintillators. Between Fig. 12 (a) and Fig. 12 (b) a difference in the the cross-talk/main signal ratio is perceivable: in particular, in the first plot (configuration c_a) the cross-talk signal amplitude is much higher than in the left figure (c_g, with two teflon layers and one aluminum layer between adjacent scintillators), where it is almost negligible with respect to the main signal.

In Fig. 13 examples of spectra of the same configurations as Fig. 12 are shown: the blue spectrum shows the amplitudes for the triggered channels, while the red spectrum shows the induced cross-talk signal amplitude; again, the cross-talk signal amplitude appears to be larger in the configuration with uncovered scintillators (Fig. 13 (a)) than in Fig. 13 (b), where the red peak is sharper and closer to zero. The function that best fits the spectra shapes such as those in Fig. 13 is a Landau function, typical of Minimum Ionizing particles as cosmic muons.

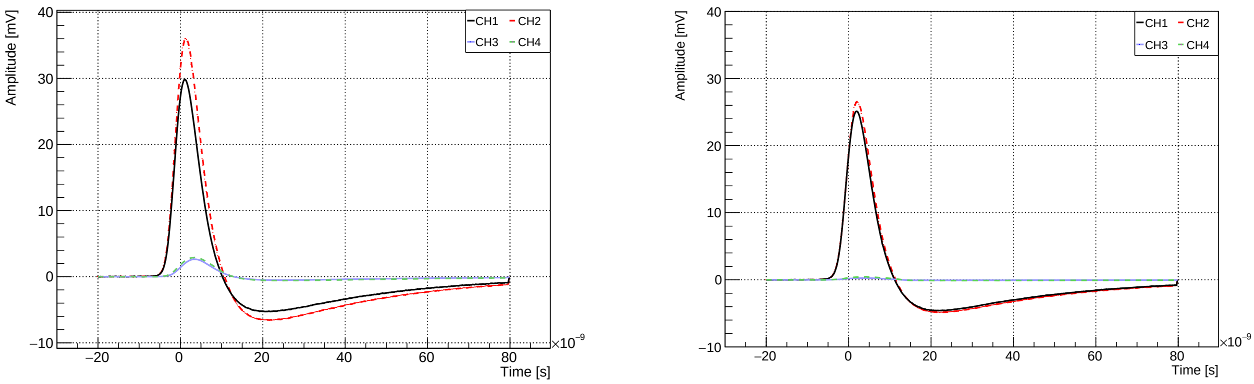

(a) (b)

Figure 12: Signals average waveforms for triggered and untriggered channels, in configurations c_a (a) and c_g (b).

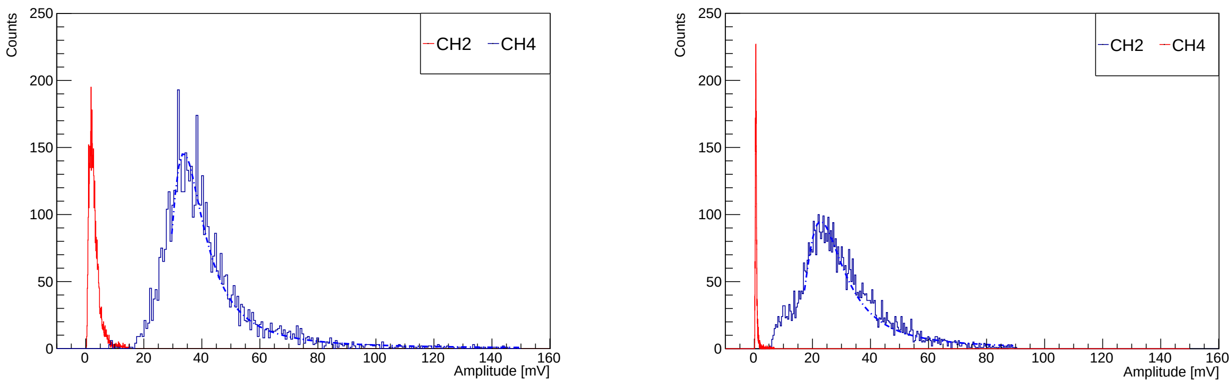

(a) (b)

Figure 13: Examples of signals amplitude spectra for triggered and untriggered channels, in configurations c_a (a), Ch2 (red) bin width 0.15 mV, Ch4 (blue) bin width 0.65 mV and c_g (b), Ch2 (red) bin width 0.02 mV, Ch4 (blue) bin width 0.4 mV. Triggered channels are fit with a Landau function.

For each configuration, the spectrum of the signals voltage amplitude was fit with a Landau distribution, while in spectra containing only background noise a gaussian fit was performed instead. The median of each distribution was retrieved from the fit function. The median was chosen as an indicative value of the central of the distribution instead of the mean, as the latter is too skewed towards the right tail and further away from the maximum value than the median. As an estimation of the distribution width, values marking the 34% of the distribution integral from each side of the median were chosen. The resulting median signal amplitudes and their 68% interval boundaries are presented in Tab. 1 for each configuration; the tabulated values are the average between the two triggered and the two non-triggered channels respectively, for each data set. The overall average ratio between the induced signal in the non-triggered channels and the main signal is also presented.

Configuration	Triggered channels	Main signal amplitude [mV]	Cross-talk signal amplitude [mV]	Ratio
a	*1-2*	34^{+13}_{-5}	$2.8^{+2.2}_{-0.8}$	$0.07^{+0.05}_{-0.02}$
	3-4	39^{+14}_{-5}	$2.3^{+1.8}_{-0.7}$	
b	*1-2*	13^{+8}_{-3}	$0.54^{+0.25}_{-0.09}$	$0.041^{+0.022}_{-0.009}$
	3-4	13^{+9}_{-3}	$0.5^{+0.1}_{-0.1}$	
c	*ext*	–	$0.50^{+0.09}_{-0.09}$	–
d	*1-2*	19^{+13}_{-5}	$0.5^{+0.1}_{-0.1}$	$0.03^{+0.02}_{-0.01}$
e	*1-2*	23^{+11}_{-4}	$0.9^{+0.8}_{-0.3}$	$0.033^{+0.025}_{-0.009}$
	3-4	31^{+14}_{-5}	$0.8^{+0.6}_{-0.2}$	
f	*1-2*	30^{+14}_{-5}	$0.8^{+0.7}_{-0.3}$	$0.028^{+0.021}_{-0.008}$
	3-4	29^{+16}_{-6}	$0.7^{+0.5}_{-0.2}$	
g	*1-2*	28^{+16}_{-6}	$0.6^{+0.3}_{-0.1}$	$0.017^{+0.009}_{-0.004}$
	3-4	37^{+16}_{-6}	$0.5^{+0.1}_{-0.1}$	

Table 1: Signal amplitude of triggered and untriggered channels and ratio between cross-talk signal and main signal for each setup configuration. For c_c, where all channels were triggered externally, no cosmic events signals are present.

The results show that the configuration with two layers of teflon and one layer of aluminum is the best solution for minimising the cross-talk between adjacent scintillators, the cross-talk being $\leq 2\%$ of the maximum signal. The setup where all the scintillators are uncovered is the one with largest cross-talk ($\approx 7\%$ of the main signal). A configuration with three layers of teflon would have further decreased the cross-talk but it did not meet the requirement of minimising the thickness between the two scintillators and a cross-talk lower than the one obtained with configuration c_g was not considered necessary. Comparing the values obtained for the cross-talk signal amplitude in the three background configurations (c_b, c_c and c_d), the signal amplitude found is approximately the same: the SiPM dark count is therefore negligible, as well as electronics cross-talk and almost all the background noise can be traced back to electronics noise. The comparison between the amplitude of the main signal and the amplitude of the cross-talk signal for each configuration is shown in Fig. 14: from (a) it is possible to deduce that again c_a is not a favorable configuration for the purpose of minimising the cross-talk, as the main signal is the highest observed but the cross-talk signal is the highest as well; on the other hand, the cross-talk signal amplitude for c_g is approximately the same obtained with the background measurements configurations (≈ 0.5 mV, the main signal amplitude still being more or less 30 mV). Fig. 14 (b) confirms that the wrapping made of two teflon layers and an aluminum layer is the best option, as the ratio cross-talk/main signal is the lowest observed (c_g).

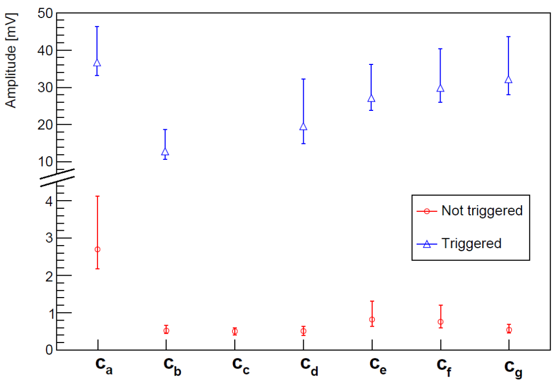

(a)

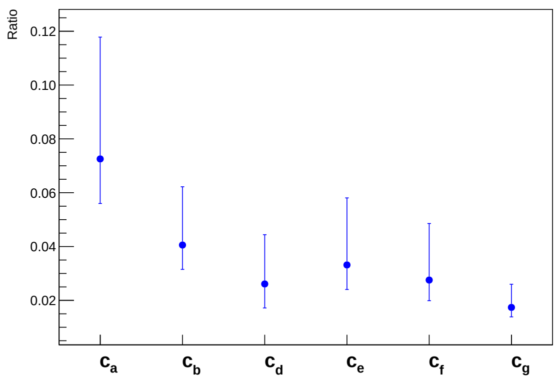

(b)

Figure 14: Mean signal amplitude for triggered channels and non triggered channels (a) and ratio of cross-talk signal amplitude over main signal amplitude (b) for the different configurations.

4.2 Response uniformity setup and analysis

The uniformity of the response inside the entire scintillation volume is a critical aspect in the study of the iMPACT project calorimeter. The detected signals amplitudes, in fact, are required to be independent from the particle passing position inside the detector volume, to avoid possible errors in the reconstruction of the particle track.

A preliminary simulation using GATE (Sec. 3.2) did show a strong dependence between the signal voltage intensity from the SiPM and the distance of the particle incident position from the SiPM, as shown in Fig. 15. Particles depositing energy in the proximity of the scintillator face where the SiPM was placed, in fact, were predicted to produce signal more than 40% higher than particles passing at the opposite end of the scintillator, the energy loss being the same.

The iLDA setup described in Sec. 3.3 was adapted to perform studies on the response uniformity in order to experimentally measure the dependence of the signal on the position, using cosmic muons. The experimental results had to be compared with the results previously obtained from the simulation, to either confirm or discard the validity of the code in reproducing this behaviour, and the experimental response curve would eventually be used as a parameterisation in future simulations of the entire apparatus.

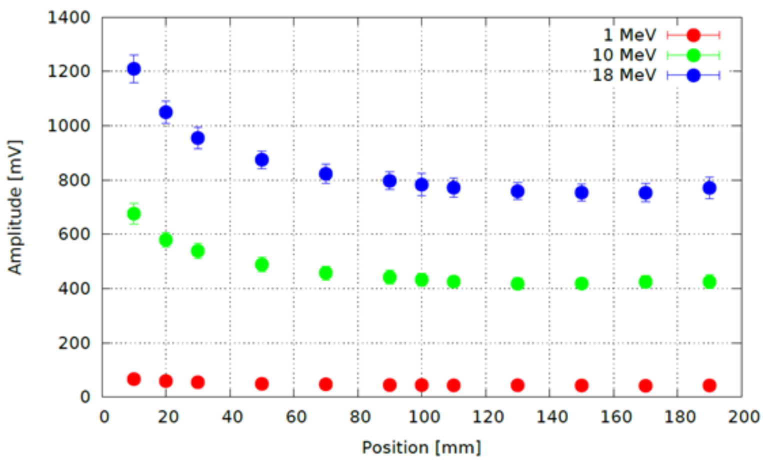

Figure 15: Simulated signal amplitude produced by monoenergetic protons, with energy 1, 10 and 18 MeV, as a function of the incident distance from the SiPM surface.

The iLDA setup for the position scan employed two scintillators, arranged perpendicularly from one another, as shown in Fig. 16. One of the two scintillators was cut to a quarter of its length, for practical reasons: the shorter scintillator could be moved along an aluminum rail, spanning the entire length of the full-size scintillator. For the read-out of the scintillator 1 a *Photomultiplier Tube* (PMT) was used, instead of a SiPM. The longer scintillator under test, the one used to measure the position dependence, was wrapped with several layers of teflon and aluminium, ensuring the best performance in photon collection. The acquisition trigger was set to accept a coincidence between the two channels, thus selecting particles passing at the chosen distance from the SiPM. Fig. 17 shows examples of spectra acquired with a PMT (a) and with a SiPM (b).

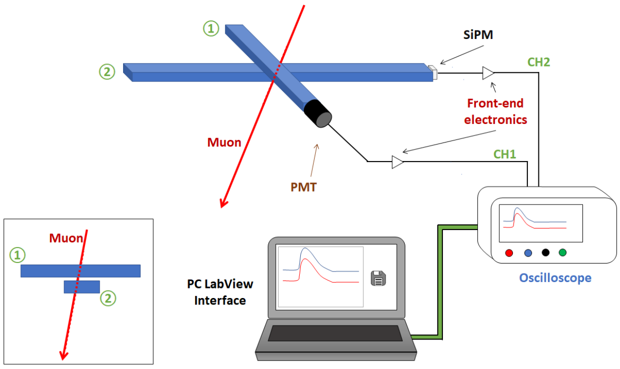

(a)

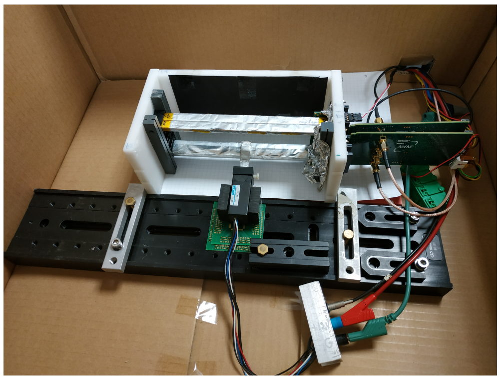

(b)

Figure 16: (a) Schematic representation of the iLDA cosmic muon desktop detector setup, used in the configuration for the response uniformity in position studies: the scintillators are labelled 1 and 2; scintillator 1 can be moved along the other one, in order to perform the position scan; in the box a horizontal view is shown; (b) a photo of the setup in the said configuration.

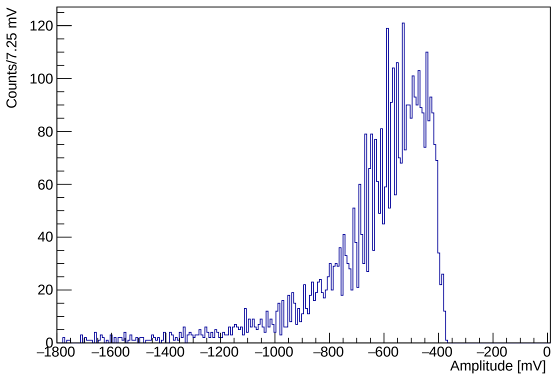

(a)

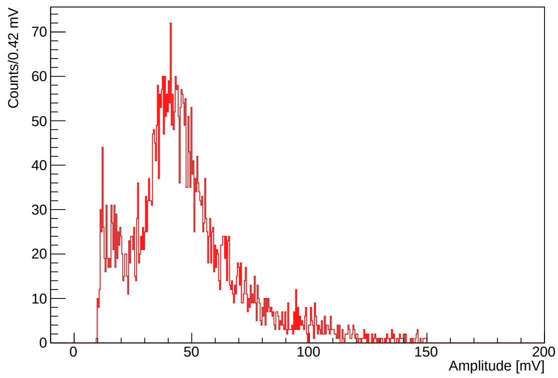

(b)

Figure 17: (a) Scintillator 1 signal amplitude spectrum, produced by a PMT (CH1) (b) Scintillator 2 signal amplitude spectrum, produced by a SiPM (CH2).

The experimental data acquired with this setup show a different result from the one obtained with the first simulation: the measured signal amplitudes for the different positions along the scintillator are compatible with each other and their distribution shows no dependence on the position, within the error bars (Fig. 18). The simulation configuration was then modified in order to find a better agreement between the prediction and the experimental results: the reflectivitys of the internal surface and the scintillator material were both increased, using values still suitable for the simulated scintillator. A recalibration of the light output was also needed, given the modification of said parameters. The

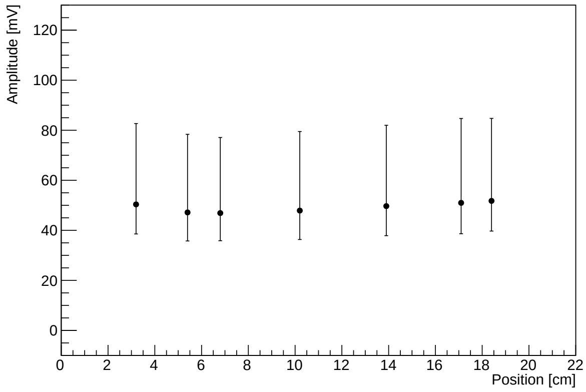

Figure 18: Measured signal amplitude as a function of the different incidence positions of the particles along the scintillator

calibration was performed using as a reference data sets obtained from a test beam performed with protons from 70 to 230 MeV [14],[20],[21]. A new simulation was run to verify whether the parameters adjustment improved the correspondence of the Monte Carlo with the experimental data. The simulation consisted of a point-like muon source (*pencil beam*) impinging on a single scintillator in a given position (Fig 21 (a)). The energy spectrum of the source was parameterised based on the realistic muons spectrum, shown in Fig. 9 (a). The incidence position of the beam could be changed along the scintillator to perform the position scan, but realistic conditions were not taken into account for what concerns the actual spatial and angular distribution of the cosmic muons. The results of the modified simulation (labelled as *Simulation v1*) are presented in Fig. 19. The simulated signals show no strong correlation between the amplitude and the passing position of the ionising particle, as observed in the experimental data. In Fig. 20 the experimental and simulation results are compared: the amplitude of the simulated signal (a) is consistently lower than the measured ones (b), while still being compatible within the error bars. The agreement between the two data sets is a remarkable results, given the fact that the calibration was performed with different particles and energy range (protons with 70 to 230 MeV, that are not considered Minimum Ionising Particles) than the one that are being simulated, muons with $E > 1$ GeV. An improved simulation (labelled as *Simulation v2*) was performed after confirming the goodness of the new parameter set, implementing a more realistic modeling of the setup. The second version of the simulation considered two scintillators, one four times longer than the other, placed perpendicularly to each other. The muon source was defined as a large

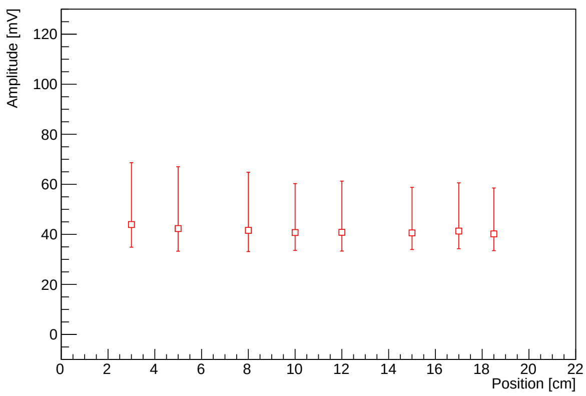

Figure 19: signal amplitude as a function of the different incidence positions of the particles along the scintillator as obtained from *Simulation v1*.

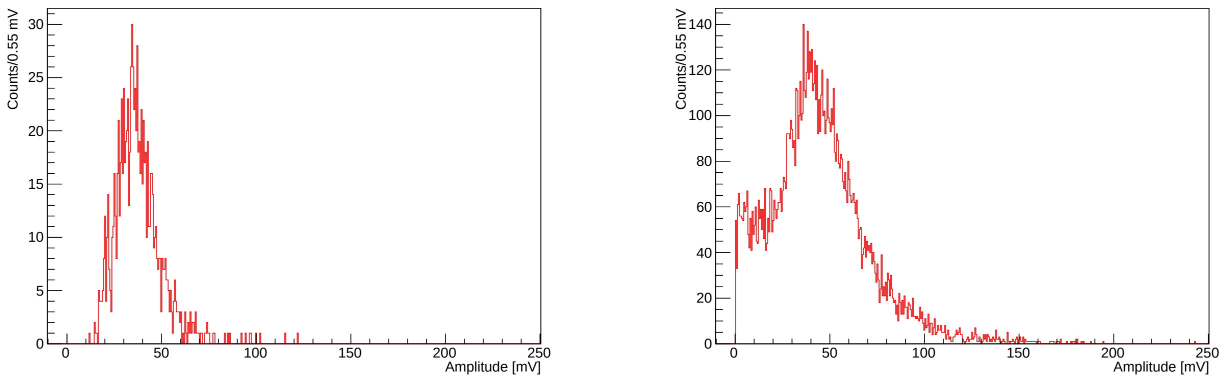

(a) (b)

Figure 20: Examples of simulated signal amplitude spectrum (a) and experimental signal amplitude spectra(b).

surface emitting isotropically towards the scintillators; the geometry of this second simulation can be seen in Fig. 21 (b). The same realistic muons energy spectrum was adopted. This conditions are still not totally realistic as they do not take into account the angular distribution of cosmic muons scaling as $\cos^2\theta$, being theta the polar angle measured from the zenith.

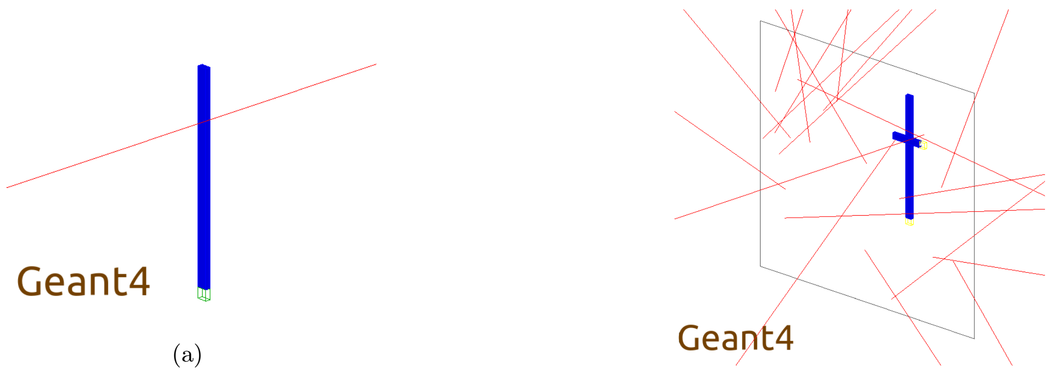

(a) (b)

Figure 21: (a) Rendering of the *simulation v1* geometry: a muon pencil beam (red) incident on a single scintillator; (b) Rendering of the *simulation v2* geometry: muons are generated from a surface (grey), two perpendicular scintillators are present.

The results of the latter simulation are presented in Fig. 22 in direct comparison with both the measurements and the previous simulation. These results are more similar to the experimental values than those obtained with *Simulation v1*: besides the nearly constant trend confirming the independence of the signal amplitude from the distance of the incident particle from the SiPM, the simulated values obtained for the signal amplitude are also more compatible with the experimental ones. This is because in this case the incident particles come from all the directions and not only perpendicular to the scintillator. When hitting the scintillator in a transverse direction, with an incidence angle $\theta \neq 90°$, the particle's path inside the detector is longer than the path of a particle with incidence angle $\theta = 90°$; the amount of energy lost in the scintillator is therefore greater and the signal amplitude is higher. The experimental results are in good agreement within the error bars with the Geant*4* based simulation, as shown in Fig. 22. Both the measurements obtained with iLDA and the improved simulation show that there is no significant dependence of the signal amplitude on the charged particle crossing position. Extending this result to the whole calorimeter volume, this study points out that the position where the ionising particle hits the scintillator is irrelevant when considering the response of the calorimeter, that can therefore be considered uniform.

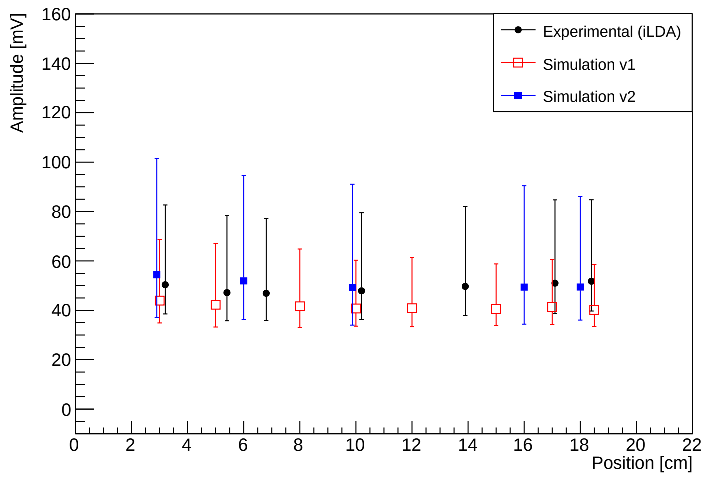

Figure 22: Comparison of the measurements with simulations: signal amplitude as a function of the different incidence positions of the particles along the scintillator.

5 Conclusions

Hadron therapy is nowadays the most effiecient way of treating a tumor, thanks to the precision it allows in targeting the volume that needs treatment limiting damages on healthy tissues. Proton Computed Tomography is an alternative to X-rays Computed Tomography that plans to use the same particles for the imaging phase and for the treatment, increasing precision and efficiency of the latter and saving time and economical resources. The slow acquisition rate of current prototypes is the main limitation preventing this technique from being clinically viable: iMPACT's scanner for pCT is designed to shorten the time for the acquisition phase making it the fastest model amongst the ones that are being developed around the world, while still being competitive for what concerns the spatial and Stopping Power resolution. To do this, iMPACT exploits some of the most recent technologies developed for particle detectors, such as monolithic Silicon pixel sensors, and Silicon Photomultipliers (SiPM).
A dedicated Data Acquisition system (iLDA) was implemented for the specific purpose of investigating the best conditions for maximising the efficiency of the setup and further characterise its components. The system exploits cosmic rays, as a reliable and free source of radiation, in particular cosmic muons, which behave as Minimun Ionising Particles.
An important question to consider in the calorimeter design and assembly is the cross-talk between adjacent scintillating elements, which needs to be minimised, without excessively affecting the material budget. After performing some measurements to take into account and estimate the contribution of the various components of the setup to the background noise (SiPMs' dark count, electronics cross-talk and electronics noise), configurations of the setup with different scintillators wrapping were investigated, finding that the best solution while avoiding an excessive thickness is a wrapping made of two layers of teflon and one layer of aluminum. Future steps would be adapting efficiently this wrapping method to the whole $8 \times 8 \times 32$ fingers calorimeter.
A second crucial aspect of characterising the calorimeter elements is monitoring their uniformity response and in particular the dependence of the generated signal amplitude on the hitting position of the ionising radiation along the finger. The Data Acquisition system was slightly modified for this study, implementing two perpendicular scintillators and a coincidence trigger. The experimental measurements showed no dependence within the error bars between signal amplitude and particles hitting position, meaning this issue does not need to be taken into account when reconstructing the particles

path inside the whole calorimeter. The experimental results was in disagreement with the simulation tool that was previously developed for the iMPACT scanner. Some of the parameters of simulation code was then modified (in particular the internal wrapping surface reflectivity and the scintillator absorption length) to match the results obtained with experimental measurements. The results of this work were therefore essential to correct the imprecise parameterisation of the Monte Carlo and will play an important role in the future of the project, as the results will be used to parameterise the responce of the whole volume of the calorimeter.

Bibliography

[1] U. Schneider, J. Besserer, P. Pemler, M. Dellert, M. Moosburger, E. Pedroni, and B. Kaser-Hotz, "First proton radiography of an animal patient", *Medical Physics*, vol. 31, no. 5, pp. 1046–1051, 2004.

[2] A. Jemal, F. Bray, M. M. Center, J. Ferlay, E. Ward, and D. Forman, "Global cancer statistics", *CA: a cancer journal for clinicians*, vol. 61, no. 2, pp. 69–90, 2011.

[3] D. Schardt, T. Elsässer, and D. Schulz-Ertner, "Heavy-ion tumor therapy: Physical and radiobiological benefits", *Reviews of Modern Physics*, vol. 82, no. 1, p. 383, 2010.

[4] D. Cussol, "Hadron therapy", in *École Joliot-Curie (30 years) "Physics at the femtometer scale"*, 2011, 46–p.

[5] W. D. Newhauser and R. Zhang, "The physics of proton therapy", *Physics in medicine and biology*, vol. 60, no. 8, R155, 2015.

[6] F. Bloch, "Zur bremsung rasch bewegter teilchen beim durchgang durch materie", *Annalen der Physik*, vol. 408, no. 3, pp. 285–320, 1933.

[7] V. Giacometti, "Modelling and improvement of proton computed tomography", Phd Thesis, PhD thesis, University of Wollongong, 2016.

[8] W. H. Bragg and R. Kleeman, "XXXIX. On the α particles of radium, and their loss of range in passing through various atoms and molecules", *The London, Edinburgh, and Dublin Philosophical Magazine and Journal of Science*, vol. 10, no. 57, pp. 318–340, 1905.

[9] J. F. Janni, "Proton Range-Energy Tables, 1 keV-10 GeV, Energy Loss, Range, Path Length, Time-of-Flight, Straggling, Multiple Scattering, and Nuclear Interaction Probability. Part I. For 63 Compounds", *Atomic data and nuclear data tables*, vol. 27, p. 147, 1982.

[10] G. Molière, "Theorie der streuung schneller geladener teilchen ii mehrfach-und vielfachstreuung", *Zeitschrift für Naturforschung A*, vol. 3, no. 2, pp. 78–97, 1948.

[11] A. Mustafa and D. F. Jackson, "The relation between X-ray CT numbers and charged particle stopping powers and its significance for radiotherapy treatment planning", *Physics in Medicine and Biology*, vol. 28, no. 2, p. 169, 1983.

[12] M. Yang, X. R. Zhu, P. C. Park, U. Titt, R. Mohan, G. Virshup, J. E. Clayton, and L. Dong, "Comprehensive analysis of proton range uncertainties related to patient stopping-power-ratio estimation using the stoichiometric calibration", *Physics in medicine and biology*, vol. 57, no. 13, p. 4095, 2012.

[13] C. Civinini, D. Bonanno, M. Brianzi, M. Carpinelli, G. Cirrone, G. Cuttone, D. L. Presti, G. Maccioni, S. Pallotta, N. Randazzo, *et al.*, "Proton computed tomography: Iterative image reconstruction and dose evaluation", *Journal of Instrumentation*, vol. 12, no. 01, p. C01034, 2017.

[14] F. Baruffaldi, "Studies for a proton tomography scanner", *University of Padova*, 2017, Master Degree thesis.

[15] V. Bashkirov, R. W. Schulte, R. Hurley, R. Johnson, H.-W. Sadrozinski, A. Zatserklyaniy, T. Plautz, and V. Giacometti, "Novel scintillation detector design and performance for proton radiography and computed tomography", *Medical physics*, vol. 43, no. 2, pp. 664–674, 2016.

[16] U. Schneider, E. Pedroni, M. Hartmann, J. Besserer, and T. Lomax, "Spatial resolution of proton tomography: Methods, initial phase space and object thickness", *Zeitschrift für Medizinische Physik*, vol. 22, no. 2, pp. 100–108, 2012.

[17] M. Goitein and M. Jermann, "The relative costs of proton and x-ray radiation therapy", *Clinical Oncology*, vol. 15, no. 1, S37–S50, 2003.

[18] P. Giubilato, W. Snoeys, S. Mattiazzo, N. Pozzobon, D. Pantano, D. Bisello, T. Kugathasan, J. Rousset, H. Mugnier, and C. M. Tobon, "Impact: Innovative pct scanner", in *2015 IEEE Nuclear Science Symposium and Medical Imaging Conference (NSS/MIC)*, IEEE, 2015, pp. 1–2.

[19] M. Mager, ALICE Collaboration, *et al.*, "ALPIDE, the Monolithic Active Pixel Sensor for the ALICE ITS upgrade", *Nuclear Instruments and Methods in Physics Research Section A: Accelerators, Spectrometers, Detectors and Associated Equipment*, vol. 824, pp. 434–438, 2016.

[20] F. Baruffaldi, "Simulations and test beam studies of the impact calorimeter", *Nuovo Cim.*, vol. 41, p. 117, 2018.

[21] N. Pozzobon, F. Baruffaldi, D. Bisello, C. Bonini, B. Di Ruzza, P. Giubilato, S. Mattiazzo, D. Pantano, L. Silvestrin, W. Snoeys, *et al.*, "Calorimeter prototyping for the impact project pct scanner", *Nuclear Instruments and Methods in Physics Research Section A: Accelerators, Spectrometers, Detectors and Associated Equipment*, vol. 936, pp. 1–4, 2019.

[22] Hamamatsu SiPM Data sheet, `http://www.hamamatsu.su/images/hamam/katalogi/mppc_kapd0002e.pdf`.

[23] Saint-Gobain BC408 Data Sheet, `http://www.crystals.saint-gobain.com/sites/imdf.crystals.com/files/documents/sgc-bc400-404-408-412-416-data-sheet.pdf`.

[24] S. Jan, G. Santin, D. Strul, S. Staelens, K. Assie, D. Autret, S. Avner, R. Barbier, M. Bardies, P. Bloomfield, *et al.*, "GATE: a simulation toolkit for PET and SPECT", *Physics in medicine and biology*, vol. 49, no. 19, p. 4543, 2004.

[25] S. Agostinelli, J. Allison, K. a. Amako, J. Apostolakis, H. Araujo, P. Arce, M. Asai, D. Axen, S. Banerjee, G. Barrand, *et al.*, "Geant4—a simulation toolkit", *Nuclear instruments and methods in physics research section A: Accelerators, Spectrometers, Detectors and Associated Equipment*, vol. 506, no. 3, pp. 250–303, 2003.

[26] M. P. Alessandro De Angelis, *Introduction to Particle and Astroparticle Physics. [Multimessenger Astronomy and its Particle Physics Foundations]*. Springer, 2015, ISBN: 9783319781808.

[27] B. Rossi, "Cosmic rays", 1964.

[28] T. C. E. Encyclopedia. (), [Online]. Available: `https://encyclopedia2.thefreedictionary.com/cosmic+rays`.

[29] P. Shukla and S. Sankrith, "Energy and angular distributions of atmospheric muons at the earth", *International Journal of Modern Physics A*, vol. 33, no. 30, p. 1 850 175, 2018.

[30] L. D. Landau, "On the energy loss of fast particles by ionization", *J. Phys.*, vol. 8, pp. 201–205, 1944.

[31] K. A. Olive, K. Agashe, C. Amsler, M. Antonelli, J.-F. Arguin, D. M. Asner, H. Baer, H. R. Band, R. Barnett, T. Basaglia, *et al.*, "Review of particle physics", *Chinese physics C*, vol. 38, no. 9, p. 090 001, 2014.